Contents lists available at ScienceDirect

Transactions of Nonferrous Metals Society of China

36(2026) 872−886

www.tnmsc.cn

Microstructure and properties of Cu−Ni−Co−Si alloy designed by cluster formula approach

Shi-fang LI [a], Zhu XIAO [a,b,*], Xiang-peng MENG [a,c], Zhou LI [a], Yan-lin JIA [a], Yan-bin JIANG [a]

[a] School of Materials Science and Engineering, Central South University, Changsha 410083, China;
[b] Key Laboratory of Non-ferrous Metal Materials Science and Engineering, Ministry of Education, Central South University, Changsha 410083, China;
[c] Ningbo Boway Alloy Material Co., Ltd., Ningbo 315135, China

---

Abstract: A Cu−1.9Ni−1.9Co−0.9Si (mass fraction, %) alloy with high strength and electrical conductivity was designed by cluster formula approach. The microstructure evolution of the alloy during thermomechanical treatment was systematically investigated. The strengthening mechanism and electrical conductivity of the alloy were discussed in detail. The optimal thermomechanical treatment process was as follows: solid solution → 80% cold rolling → (450 °C, 4 h) aging → 50% cold rolling → (400 °C, 4 h) aging. The designed alloy achieved excellent comprehensive properties with a microhardness of HV 260, a yield strength of 843 MPa, a tensile strength of 884 MPa, and an electrical conductivity of 42.6%(IACS). Compared to direct aging treatment, the designed alloy subjected to multi-stage thermomechanical treatment had refined grains, high density of dislocations, and accelerated of precipitation of $(Ni,Co)_2Si$ precipitates. High strength was mainly attributed to the combined effect of dislocation strengthening, work hardening and sub-grain strengthening, while good electrical conductivity was maintained through the precipitation of the large number of nanoparticles.

Keywords: Cu−Ni−Co−Si alloys; cluster formula approach; thermomechanical treatment; microstructure; strengthening mechanism

---

1 Introduction

Cu−Ni−Si alloys have been widely used as integrated circuit lead frames and electronic component connectors due to their high strength, good electrical conductivity, and good anti-stress relaxation properties [1,2]. As typical precipitation-strengthened copper alloys, the excellent comprehensive performance of Cu−Ni−Si alloys was attributed to nanoparticles precipitated from supersaturated solid solution during aging treatment [3,4]. Nano-scale precipitates hindered dislocation movement, thereby improving mechanical properties [5]. Additionally, the precipitation process consumed solute atom concentration and weakened the electron scattering, resulting in an increase in electrical conductivity [6]. The precipitates characteristics (e.g., type, size, volume fraction, and distribution) were critical in determining the effectiveness of precipitation strengthening [7]. Thus, alloy design with modifying precipitates characteristics was an effective method to achieve high-performance copper alloys [8].

There have been numerous reports on the composition design of Cu−Ni−Si alloys [9]. LI et al [10] investigated the microstructure and properties of a series of Cu−Ni−Si alloys with different Ni/Si mass ratios, concluding that Cu−Ni−Si alloys with Ni/Si mass ratios close to 4−5 (atomic ratio close to 2) presented good comprehensive properties. Additionally, several researchers have investigated

---

Corresponding author: *Zhu XIAO, Tel: +86-13974910804, E-mail: xiaozhumse@163.com
https://doi.org/10.1016/S1003-6326(25)67003-8
Received 14 June 2024; accepted 20 March 2025

the effect of microalloying elements in Cu−Ni−Si alloys, including Cr [11,12], Ti [13,14], Nb [15], Al [16], Zr [17,18], Ag [19], and notably Co [20−23]. The incorporation of Co formed orthorhombic δ-(Ni,Co)$_2$Si, suppressing spinodal decomposition process [24] and promoting the growth of the precipitates [22]. Cu−Ni−Co−Si alloys (ASTM, C70350) were developed by substituting some Ni with Co in Cu−Ni−Si alloys (ASTM, C70250). The mechanical properties and electrical conductivity of C70350 alloys were better than those of C70250 alloys [25]. LI et al [26] prepared a series of Cu−Ni−Co−Si alloys with varying Ni/Co mass ratios to study the effect of Ni/Co ratio on mechanical properties and electrical conductivity of the alloys. This experimental exploration made it hard to allow for the optimization of alloy composition to achieve the desired properties, highlighting the drawbacks of traditional trial-and-error method in terms of inefficiency and high cost.

A cluster formula approach has been proposed to serve the development of alloys, which has been successfully applied in the compositional design of Cu−Ni system alloys [27−29]. For instance, a $[(Fe_{0.7}Mn_{0.25})_1Ni_{12}]Cu_{30.3}$ cupronickel alloy was developed using the cluster formula approach, exhibiting higher corrosion resistance compared to commercial C71500 alloys [27]. In the compositional design of precipitation-strengthened Cu−Ni−Sn alloys, a $\{[Cu-Cu_{12}]Cu_3\}_4\{[Sn-Ni_{12}]Sn_3\}$ alloy (Cu−13Ni−9Sn, wt.%) with superior conductivity and hardness compared with C72900 alloy (Cu−15Ni−8Sn, wt.%) was obtained [28]. Similarly, the $[(Ni,Si,M)_1-Cu_{12}]Cu_3$ (M=Cr, Fe, Mo, Zr) cluster formula approach was employed in Cu−Ni−Si alloys to achieve high performance [29]. Above all, the effective application of cluster formula approach reduced designing time and costs in alloys development. However, there existed a notable scarcity in applying the cluster formula approach to design copper alloys with high strength and conductivity. Besides, it was hard to use the cluster formula approach to design the processing parameters of high-performance alloys, exposing limitations in evaluating the properties of the alloy. Hence, the investigation of the cluster formula approach in combination with multi-stage thermomechanical treatment is of great significance for the preparation of high-performance copper alloys.

In this work, a Cu−Ni−Co−Si alloy was designed using the cluster formula approach, and the alloy sheet was produced by multi-stage thermomechanical treatment. The microstructure, mechanical properties, and electrical conductivity of the alloy were thoroughly investigated under various thermomechanical treatment processes. The cluster formula approach was used to design the composition of the Cu−Ni−Co−Si alloy, and the impact of thermomechanical treatment on its properties was extensively discussed. A compositional design strategy for Cu−Ni−Co−Si alloys was formulated, offering valuable guidance for the development of high-performance Cu−Ni−Co−Si alloys.

2 Alloy design and experimental methods

2.1 Cluster formula approach design of alloy

For typical precipitation-strengthened Cu−Ni−Si alloys, the formation of a high-purity solid solution was a prerequisite to achieve high performance [29]. The solute atoms exhibited a chemically short-range ordered distribution, and long-range still maintained the matrix structure in solid solution. This was the basis for the cluster formula to design stable solid solution [30]. The cluster type, as a basic molecule-like structure unit in solid solution, which was the same as the unit cell, was the most basic geometrical unit for describing crystals in traditional crystallography [28].

The cluster formula could be described as a structural unit of a first-neighbor cluster plus a number of second-neighbor glue atoms, expressed as [cluster](glue atoms)$_x$ [31]. The cluster and number of glue atoms (x) need to be determined as follows:

(1) Cluster structure: The cluster represented a generalized nearest-neighbor coordination polyhedron with a central atom (M). There were 12 atoms (polyhedral shell atoms) in the nearest-neighbor around central atom M for copper alloys (FCC structure), namely a cube-octahedron cluster $[M-Cu_{12}]$ with a coordination number of 12, as shown in Fig. 1(a).

(2) Central atom M: There was strong interaction between central atom M and polyhedral pellet atoms, and the interaction was reflected in the mixing enthalpy [28,31]. According to the mixing enthalpy of matrix Cu with alloying elements (ΔH_{Cu-Ni}=0.04 eV, ΔH_{Cu-Co}=0.06 eV, and ΔH_{Cu-Si}=

−0.19 eV [32]), there was a strong interaction between Si and Cu. Si, as the central atom, was attached to Cu. Moreover, Co and Ni had negative mixing enthalpies with Si and positive mixing enthalpies with Cu ($\Delta H_{\text{Ni-Si}}$=−0.41 eV, and $\Delta H_{\text{Co-Si}}$= −0.39 eV [32]), indicating that Ni and Co were in close proximity to Si and away from Cu. Considering (Ni,Co)/Si molar ratio close to 2 with good properties [26], the cluster was given as $[(\text{Ni,Co})_{2/3}\text{Si}_{1/3}-\text{Cu}_{12}]$.

(3) Number of glue atoms [30]: Cu was the glue atoms, acting as a connection between clusters. The number of glue atoms x decided the stability of the cluster formula structure. Based on the effective pair potential function (Fig. 1(b)), clusters losing valence electrons preferentially populated negative potential region (Trough: $r_1=1.25\lambda_{\text{Fr}}$), and the connecting atoms were located in the positive charge region (peak: $r_{1.5}=1.75\lambda_{\text{Fr}}$). r_1 corresponded to the nearest-neighbor distance ($r_1=a/\sqrt{2}$), and $r_{1.5}$ corresponded to the radius of cluster formula (The theoretical radius of cluster formula was equal to $1.76\lambda_{\text{Fr}}$ (the first charge-neutral position) interfered by near-neighbor clusters). The total number of atoms in a cluster formula structure was $(4\pi/3)(1.76\lambda_{\text{Fr}})^3\rho_a\approx16$, i.e., x value was given to be 3.

In conclusion, the stabilized cluster formula for the Cu−Ni−Co−Si alloy was expressed as $[(\text{Ni,Co})_{2/3}\text{Si}_{1/3}-\text{Cu}_{12}]\text{Cu}_3$ (Cu−1.9Ni−1.9Co−0.9Si, wt.%). The main chemical composition of the commercial Cu−Ni−Co−Si alloys (ASTM, C70350) was: 1.0−2.5 wt.% Ni, 1.0−2.0 wt.% Co, and 0.5−1.2 wt.% Si [33], with the popular alloys being Cu−1.5Ni−1.1Co−0.6Si. The composition of the designed alloy by cluster formula approach was situated in this range, but it had higher content alloying elements than the popular Cu−1.5Ni−1.1Co−0.6Si alloys.

Equilibrium structure was the basis of alloy design and a prerequisite for designing high-performance precipitation-strengthened alloys. The equilibrium structure of the cluster-designed alloys was discussed based on thermodynamic data. From the binary phase diagrams of Cu−Ni, Cu−Co, and Cu−Si (Springer materials data source), Ni was infinitely dissolved in Cu, while Co and Si had a certain degree of solid solubility in Cu (the solubility of Co and Si in Cu at 950 °C was approximately 3.5 wt.%, and 5.0 wt.%, respectively). It was inferred that the designed alloy would be a single solid solution at high temperatures. The isothermal cross-sectional phase diagrams of the Cu−Ni−Si, Cu−Ni−Co, and Cu−Co−Si ternary alloys at 950 °C were calculated by Thermo-Calc software, as shown in Figs. 2(a−c), respectively. With Ni (1.9 wt.%), Co (1.9 wt.%) and Si (0.9 wt.%) contents, the compositional points fell within the single-phase (α-solid solution, FCC) region of the Cu−Ni−Si and the Cu−Ni−Co systems, respectively, while belonged to the two-phase (FCC+Co_2Si) region of the Cu−Co−Si system. The formation enthalpies of Ni_2Si, Co_2Si, and $(\text{Ni,Co})_2\text{Si}$ were similar (−30.58, −29.06 and −29.85 eV, respectively [3]). The interaction among Ni, Co, and Co affected the equilibrium structure of the alloys, necessitating further consideration of the phase structure of the tetradentate alloys as well. Figure 2(d) shows the variation of phase fraction of the designed alloy as a

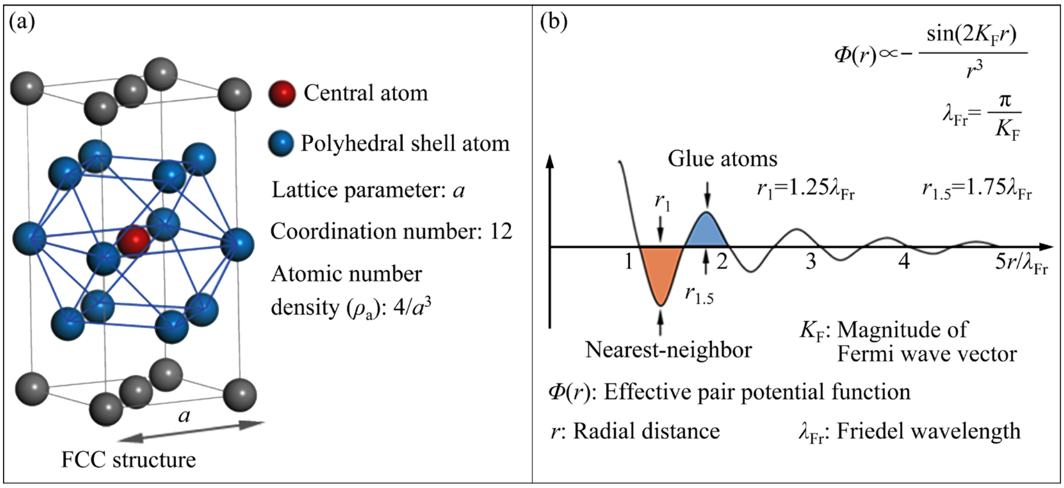

Fig. 1 Schematic diagram of Cu−Ni−Co−Si alloy cluster formula design: (a) Cluster structure of Cu matrix; (b) Effective pair potential function [30]

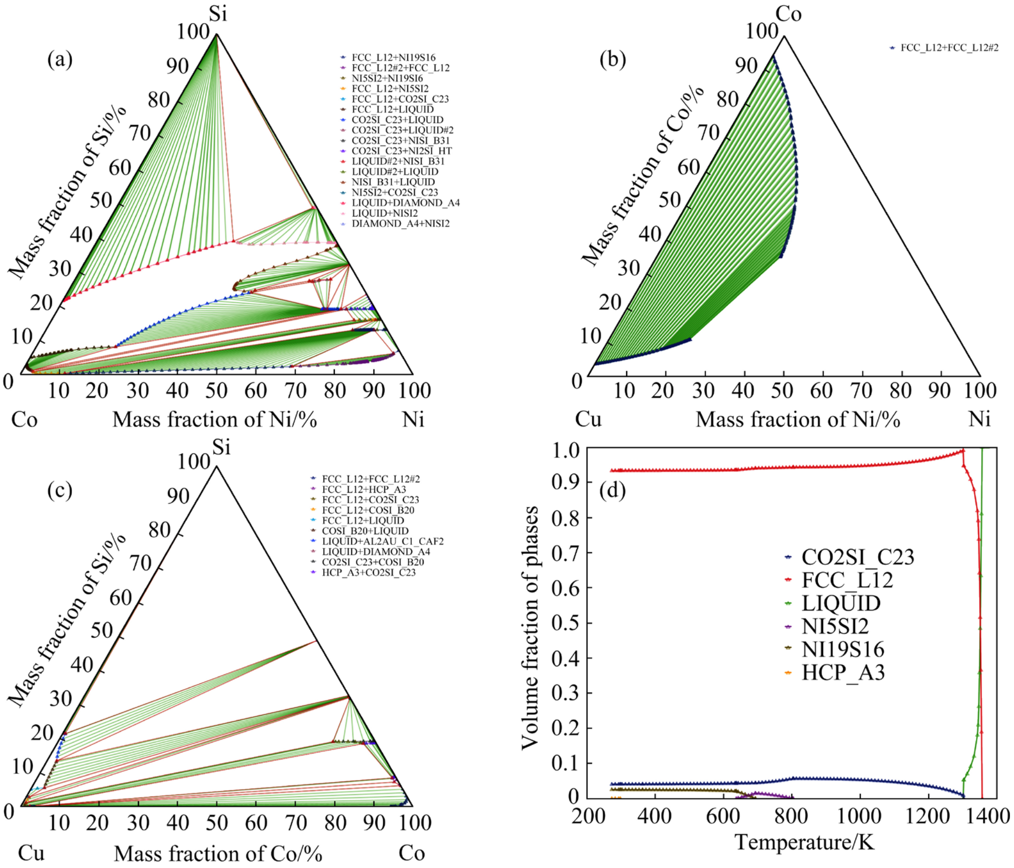

Fig. 2 (a−c) Calculated isothermal sections of Cu−Ni−Si, Cu−Ni−Co and Cu−Co−Si systems at 950 °C, respectively; (d) Phase fraction of designed alloy versus temperature

function of temperature. The designed alloy had mainly FCC structure and tiny amount of Co_2Si phase after high temperature solid solution treatment, which was similar to that reported by WANG et al [34].

2.2 Alloy preparation

The Cu−Ni−Co−Si alloy was prepared by vacuum intermediate frequency induction furnace, with the raw materials of pure Cu, Ni, Co, and Si. The chemical composition of the alloy was measured by a SPECTROBLUE inductively coupled plasma optical emission spectrometer (ICP-OES), as shown in Table 1. The ingot was subjected to homogenization at 950 °C for 4 h, and then immediately underwent hot rolling with 70% reduction. The hot-rolled plate was solid-solution treated at 950 °C for 2 h, followed by quenching in water. Finally, samples were produced from the solid solution state (SSS) plate subjected to direct aging treatment (DAT) and multi-stage thermomechanical treatment (TMT) with cold rolling (CR) and aging alternately, as listed in Table 2.

Table 1 Chemical composition of Cu−Ni−Co−Si alloy

Cluster formula	Alloy composition/wt.%	Measured content/wt.%			
		Ni	Co	Si	Cu
$[(Ni,Co)_{2/3}Si_{1/3}-Cu_{12}]Cu_3$	Cu−1.95Ni−1.96Co−0.93Si	1.91	1.93	1.01	Bal.

Table 2 Process of sample preparation

Heat treatment	Process
Direct aging treatment (DAT)	SSS + aging at 400/450/500 °C for different time
First-stage TMT (FTMT)	SSS + 80% CR+ aging at 400/450/500 °C for different time
Second-stage TMT (STMT)	Selected FTMT + 50% CR+ aging at 300/350/400 °C for different time

2.3 Properties tests

The Vickers microhardness of the samples was tested by an HV−5 hardness tester with a load of 0.5 kg and a dwelling time of 15 s. The hardness of each sample was averaged from five tests at different locations. The electrical conductivity of the samples with a size of 15 mm × 15 mm was measured by an eddy-current conductivity meter (SIGMASCOPE SMP350) with the international annealed copper standard (%(IACS)) as a reference. An Instron 5565 universal testing machine equipped with an Instron video extensometer was employed to carry out room temperature tensile tests on the samples at a tensile rate of 1 mm/min. The dimensions of the dog-bone-shaped flat tensile samples were 40 mm × 6 mm × 1 mm. Tensile tests were performed three times and the average value was taken as the mechanical properties of the samples.

2.4 Microstructure characterization

The structure of the samples was identified using a D/Max 2550VB X-ray diffraction (XRD) within a scanning range of 20°−100° and a scanning speed of 4 (°)/min. An MIRA4 LMH field emission scanning electron microscope (SEM) was used to observe the fracture morphology of the tensile samples. An SEM equipped with a NordlysMax2 electron backscatter diffraction (EBSD) detector was used to obtain crystallographic data from the samples. The EBSD samples were prepared by mechanical polishing followed by Ar-ion thinning. An FEI Talos F200x transmission electron microscope (TEM) was employed to observe the microstructure of the samples and analyze the structure of precipitated phases.

3 Results

3.1 Hardness and electrical conductivity

Figure 3 shows the variation in microhardness and electrical conductivity of the alloys after DAT and multi-stage TMT. At a given aging temperature, the microhardness initially increases to a peak before declining with prolonged aging time, while the electrical conductivity increases rapidly in the early stage of aging and then stabilizes with further aging. The variation in hardness corresponds to the generation and coarsening of precipitates, with generation prevailing in the early stage of aging and coarsening dominating in the later stages [35]. Similarly, the variation in conductivity refers to the precipitation kinetics, with rapid precipitation in the early stage of aging and limited precipitation in the late aging stage. Higher aging temperature results in shorter time to reach peak microhardness and faster increase in conductivity. The optimal aging conditions for achieving desirable comprehensive properties (product of microhardness and electrical conductivity) after DAT, FTMT and STMT are (500 °C, 480 min), (450 °C, 240 min), and (400 °C, 240 min), respectively, with corresponding microhardness and electrical conductivity values of HV 235, 38.7%(IACS), HV 247, 36.1%(IACS) and HV 260, 42.6%(IACS). Compared to DAT, multi-stage TMT enhances the combined properties of microhardness and electrical conductivity. Selected samples from the aforementioned DAT, FTMT, and STMT treatments with desirable comprehensive properties (labeled as selected-DAT, selected-FTMT, and selected-STMT) are further analyzed.

3.2 Tensile properties

Figure 4 shows typical engineering stress−strain curves and mechanical properties of alloys in different states. For the multi-stage TMT samples, there is a noticeable increase in strength and a sharp decrease in elongation compared to the SSS samples. The yield strength increases from (509±17) MPa for the selected-DAT samples to (843±7) MPa for the selected-STMT samples, while the corresponding elongation decreases from (10.3±1.9)% to (3.1±1.2)%. Figure 5 shows the fracture morphologies of tensile samples in different states at room temperature. Plethora dimples are observed, showing typical ductile fracture behavior. The dimensions of dimples decrease for samples after multi-stage TMT, aligning with the reduced elongation.

3.3 Microstructure

Figure 6 shows the XRD patterns of samples in different states. The diffraction peaks corresponding to the marked Cu matrix and the precipitates are evident. The precipitates, identified as $(Ni,Co)_2Si$, exhibit similar diffraction peaks to Ni_2Si and Co_2Si, which have orthorhombic structure with comparable lattice parameters (Ni_2Si: a=0.706 nm, b=0.499 nm, c=0.372 nm; Co_2Si: a=0.710 nm, b=0.491 nm, c=0.378 nm [22]). The intensity of diffraction peaks, primarily attributed to the precipitates, gradually increases after multi-stage TMT, indicating an increase of the content of precipitates.

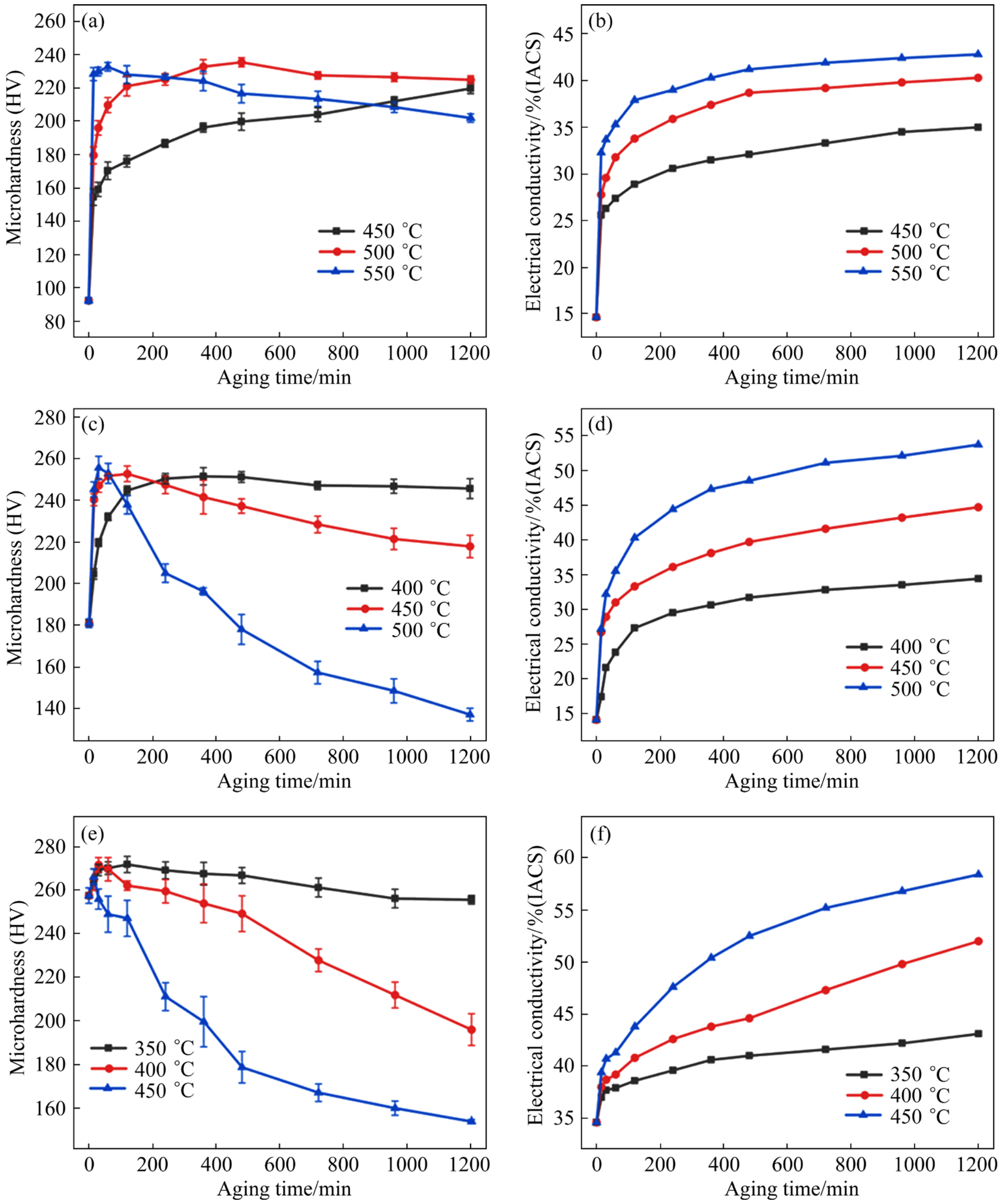

Fig. 3 Microhardness (a, c, e) and electrical conductivity (b, d, f) of alloys after DAT and multi-stage TMT: (a, b) DAT; (c, d) FTMT; (e, f) STMT

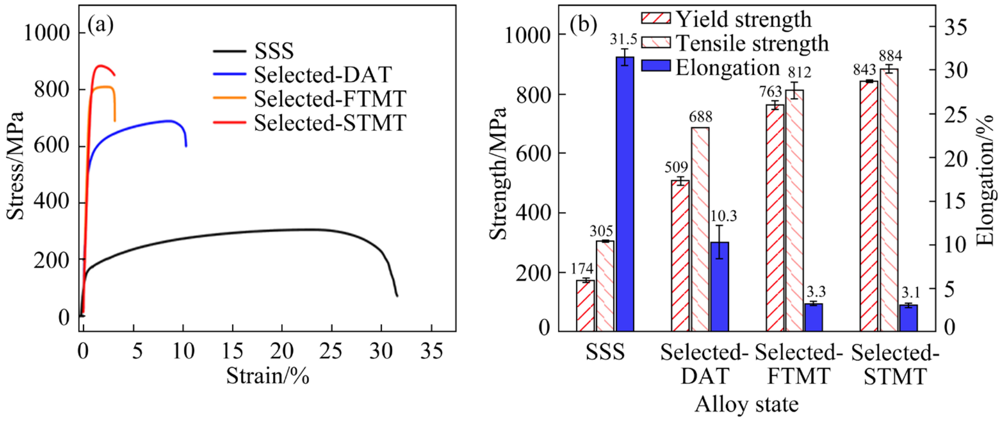

Fig. 4 Typical engineering stress−strain curves (a) and corresponding mechanical properties (b) of alloys in different states

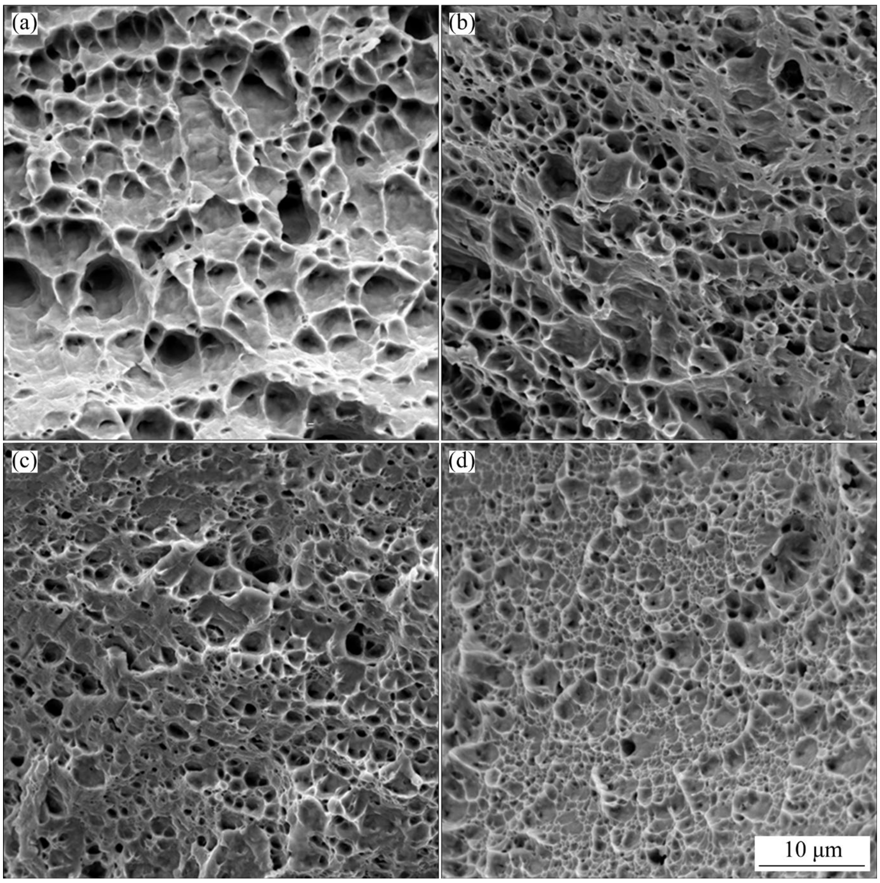

Fig. 5 Fracture morphologies of tensile samples in different states: (a) SSS; (b) Selected-DAT; (c) Selected-FTMT; (d) Selected-STMT

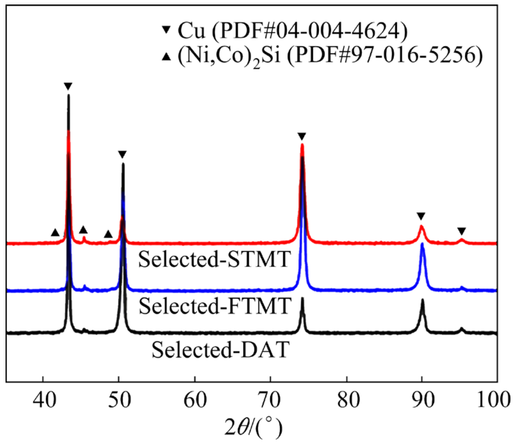

Fig. 6 XRD patterns of samples in different states

Figures 7(a−c) show inverse pole figure (IPF) coloring maps of samples in different states. The grains in the selected-DAT sample appear equiaxed with numerous twin boundaries, and the grain orientation distribution is relatively random. After TMT, the grains elongate along the rolling direction, showing fibrous structure. Excessive green and blue areas are evident in the selected-FTMT and selected-STMT samples, indicating grain rotation towards ⟨110⟩ and ⟨111⟩. Additionally, fine polygonized grains are observed in some areas, suggesting a recrystallisation process. Figures 7(d−f) and (g−i) show the orientation distribution function (ODF) sections (φ_2=0°, 45°, 65°) and texture component (TC) distributions of the samples in different states, respectively. Referring to typical face-centered cubic (FCC) crystal system ODF sections [36], the selected-DAT sample presents R-Cube texture and G/B texture with a content of 5.9% and 3.6%, respectively. The sample subjected to FTMT shows significant R/B and S deformed textures at 15.7% and 9%, respectively. Subsequent to STMT, G/B texture shifts to a stable Brass texture, and the density of S texture increases. A low density of Cube recrystallization texture is also observed. It has been revealed that grains close to the [111] crystal plane exhibit high strength with a low Schmid factor value, whereas grains close to the [100] crystal plane have low strength [37]. This phenomenon explains the increase in hardness of the samples subjected to TMT.

Figures 8(a−c) show bright field (BF) images of the selected-DAT sample. A large number of fine

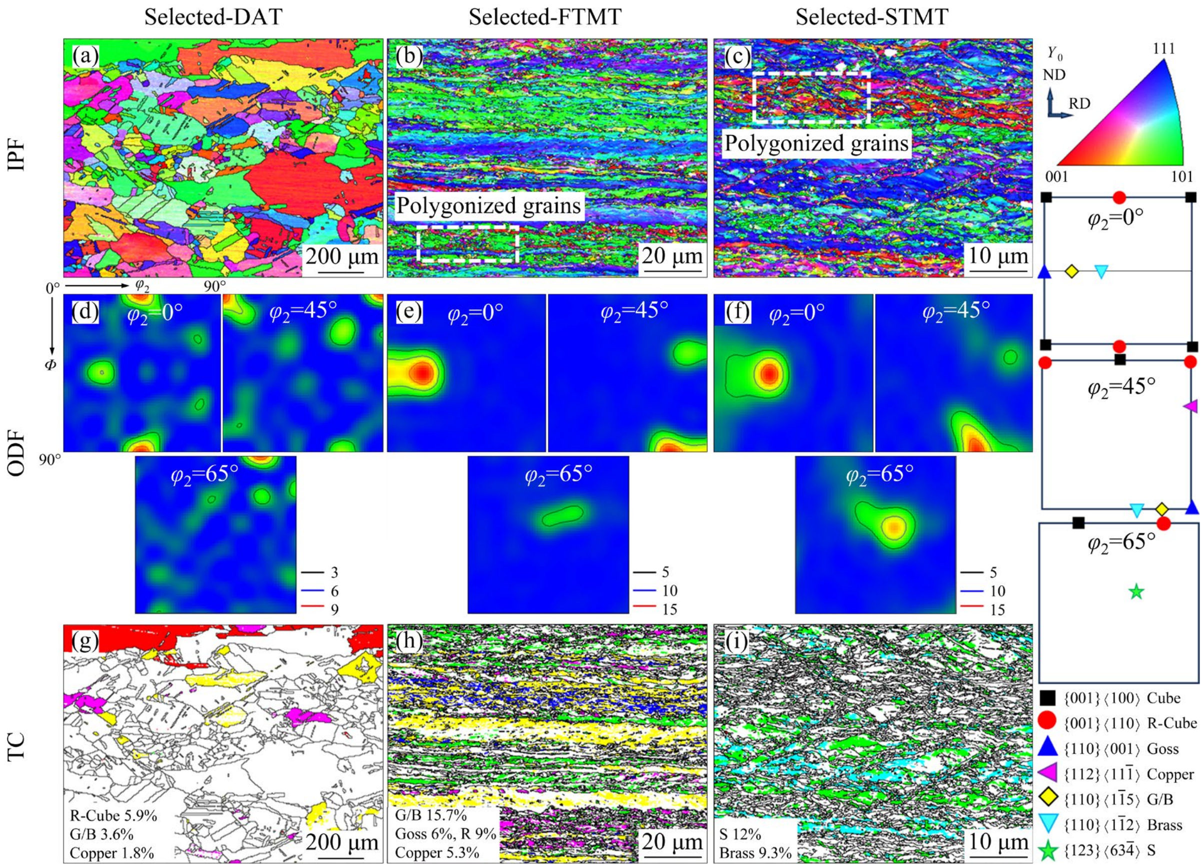

Fig. 7 EBSD maps of samples in different states: (a−c) Inverse pole figure (IPF); (d−f) Orientation distribution function (ODF); (g−j) Texture component (TC)

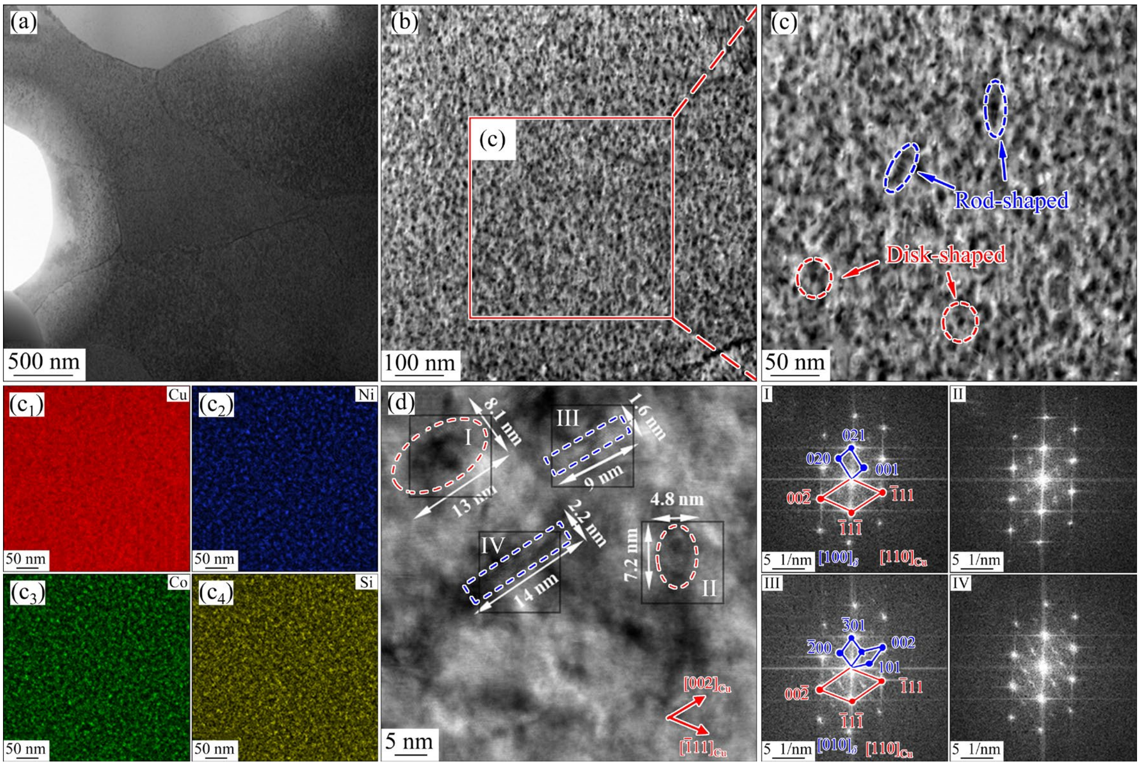

Fig. 8 TEM images of selected-DAT sample: (a, b, c) BF images; (c_1−c_4) EDS mappings of (c); (d) HRTEM image and FFT patterns of Zones I−IV

precipitates are uniformly dispersed in Cu matrix. It can be observed that nano-scale precipitates with the strain contrast have a zero-contrast line in Fig. 8(c), indicating that these precipitates are completely coherent with Cu matrix. The precipitates appear as disk-shaped and rod-shaped morphologies. Figures 8(c_1−c_4) show the corresponding energy dispersive spectrometer (EDS) analysis results of Fig. 8(c), reflecting that the precipitates mainly consist of Ni, Co, and Si. Figure 8(d) shows the high resolution TEM (HRTEM) image and fast Fourier transformation (FFT) patterns with the beam direction along $[110]_{\mathrm{Cu}}$ zone axis. The precipitates are identified as δ-$(\mathrm{Ni,Co})_2\mathrm{Si}$, as confirmed by EDS mapping and FFT patterns. The average size of the precipitates is approximately 10 nm. Different shapes of precipitates are mainly related to different growth directions, namely growth along the direction of low energy [20]. The crystal orientation relationships of the disk-shaped precipitates (Zones I and IV) and rod-shaped precipitates (Zones II and III) with the Cu matrix are $(021)_{\delta_1}//(1\bar{1}1)_{\mathrm{Cu}}$, $[100]_{\delta_1}//[110]_{\mathrm{Cu}}$ and $(\bar{3}01)_{\delta_2}//(1\bar{1}1)_{\mathrm{Cu}}$, $[010]_{\delta_2}//[110]_{\mathrm{Cu}}$, respectively, which are in agreement with the available reports [20].

Figure 9 shows TEM images of the selected-FTMT sample. There are numerous dislocation configurations in the sample, such as dislocation tangles, dislocation walls, and dislocation cells. These defects are a representation of work hardening. Additionally, the interaction between precipitates and dislocations is also observed in Fig. 9(b), which is responsible for aging strengthening. The precipitates exhibit heterogeneous dimensions, with large and small sizes corresponding to coarsened precipitates and freshly generated ones, respectively. The average particle size of precipitates in the selected-FTMT sample is approximately 13 nm, significantly larger than that of the selected-DAT sample. Figures 9(c, e) show HRTEM images of larger-size precipitates. It is worth noting that the growth of precipitates leads to the damage of the coherent relationship between the precipitates and Cu matrix.

Figure 10 shows TEM images of the selected-STMT sample. A reduced dislocation density within the intracellular region tends to be pure and the thinning of the cell wall tends to be polygonized in the selected-STMT sample, suggesting a typical recovery process. Compared to the selected-FTMT sample, the selected-STMT sample has a higher dislocation density and more significant interaction between precipitates and dislocations. The size of the precipitates further increases with an average particle size of about 27 nm. The coarsening of precipitates plays the dominant role from interfacial

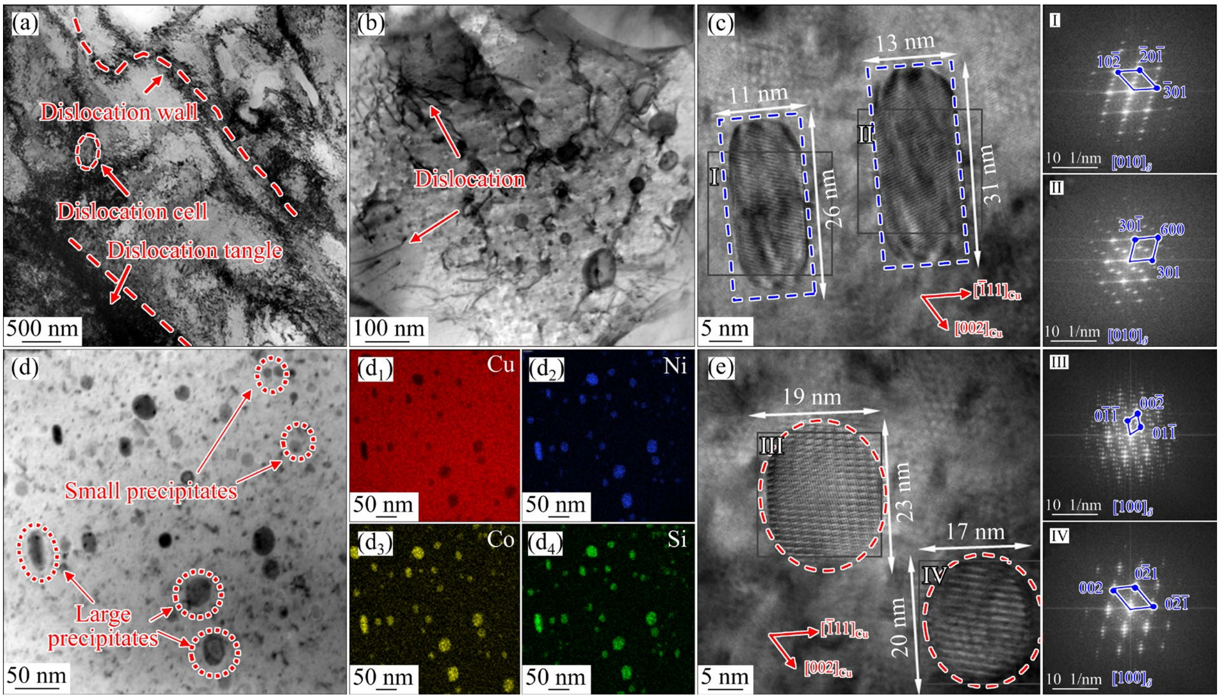

Fig. 9 TEM images of selected-FTMT sample: (a, b, d) BF images; (d_1−d_4) EDS mappings of (d); (c, e) HRTEM image and FFT patterns of Zones I−IV, respectively

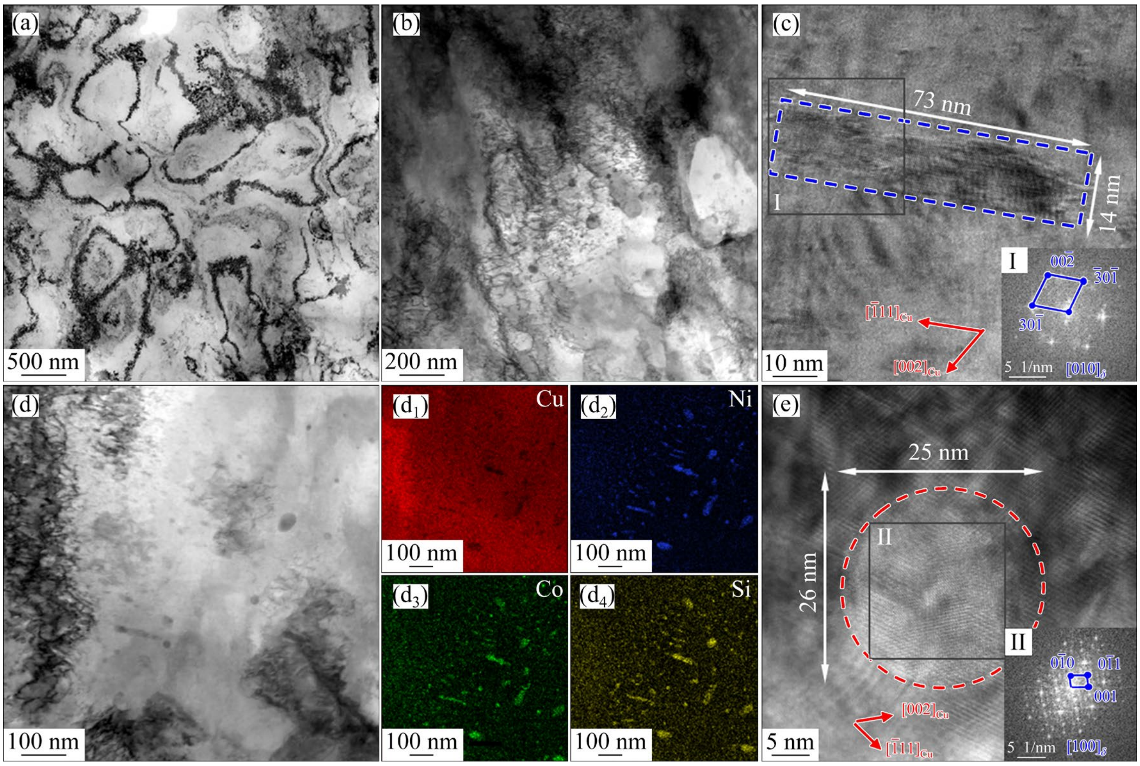

Fig. 10 TEM images of selected-STMT sample: (a, b, d) BF images; (d_1−d_4) EDS mappings of (d); (c, e) HRTEM image and FFT pattern of Zones I and II

energy to strain energy, leading to the incoherence of larger-size precipitates with Cu matrix.

4 Discussion

The process is also a crucial factor to significantly consider the properties of Cu−Ni−Co−Si alloys. The designed alloy is subjected to the multi-stage TMT, progressively improving its comprehensive performance (selected-DAT < selected-FTMT < selected-STMT). The first cold rolling deformation leads to numerous dislocations, improving the strength of the alloy. Besides, these defects accelerate precipitation during aging treatment, thus increasing the number of precipitates. The formation of precipitates simultaneously improves both mechanical properties and electrical conductivity. The precipitates developed in the first-stage TMT play a significant role in the second cold rolling process, hindering the movement of dislocations and grain boundaries, and enhancing the work-hardening effect. The precipitates associated with high deformation stored energy continue to precipitate during subsequent aging treatment, further improving the properties of the alloy. The designed alloy is subjected to multi-stage TMT, resulting in grain refinement, increased dislocation density and precipitates. The optimal multi-stage thermomechanical treatment to obtain excellent comprehensive properties is as follows: solid solution → first cold rolling by 80% → aging at 450 °C for 240 min → second cold rolling by 50% → aging at 400 °C for 240 min. The selected-STMT sample achieves a yield strength of 843 MPa, a tensile strength of 884 MPa, and an electrical conductivity of 42.6%(IACS). The effects of multi-stage TMT on mechanical properties and electrical conductivity are discussed.

4.1 Effect of multi-stage TMT on mechanical properties

The strength is derived from precipitation strengthening, strengthing caused by the work hardening, sub-grain strengthening and solid solution strengthening [26]. The strength of the alloys (σ_{alloy}) can be expressed as follows [6,38]:

$$\sigma_{alloy}=\sigma_0+\Delta\sigma_{Dis}+\Delta\sigma_G+\Delta\sigma_p+\Delta\sigma_s \quad (1)$$

where σ_0 is the strength of Cu matrix (60 MPa [6]), $\Delta\sigma_{Dis}$ is the strengthening caused by work hardening,

$\Delta\sigma_{\mathrm{G}}$ is the sub-grain strengthening, $\Delta\sigma_{\mathrm{p}}$ is the precipitation strengthening, and $\Delta\sigma_{\mathrm{s}}$ is the solid solution strengthening. For the precipitation-strengthened alloys, the contribution of solid solution strengthening to the strength of Cu−Ni−Co−Si alloys is limited and negligible [39,40].

The alloy is deformed by cold rolling to introduce a large number of dislocations, as shown in Fig. 8(a). The interaction of dislocations, such as pile-up, entanglement, and jog impedes movement, increasing the strength of the alloy. The strengthening caused by work hardening can be expressed by the Bailey−Hirsch equation [40]:

$$\Delta\sigma_{\mathrm{Dis}}=aMGb\sqrt{\rho} \tag{2}$$

$$\rho=\frac{16.1\varepsilon^2}{b^2} \tag{3}$$

where a is a constant (0.26 [40]), M is the Taylor factor (3.08 [40]), G is the shear modulus (44 GPa, [40]), b is the magnitude of Burger vector (0.255 nm [40]), ρ is dislocation density, and ε is micro-strain obtained from XRD result, as shown in the following equation [6,41]:

$$\varepsilon=\frac{\beta}{4\tan\theta} \tag{4}$$

where β is the FWHM of XRD peak, and 2θ is the diffraction angle. The micro-strain ε of the selected-STMT samples is 0.248. The dislocation density and dislocation strengthening contribution of the selected-STMT samples are obtained to be $1.6\times10^{15}\ \mathrm{m}^{-2}$ and 359 MPa, respectively.

Additionally, the conventional grains are fragmented and numerous substructures are formed during cold rolling. Dislocation entanglement forms a dislocation cell consisting of a cell wall with high dislocation density and an intracellular region of low dislocation density. The sub-grains with nearly dislocation-free intracellular regions and thinned cell walls are formed as a result of recovery during aging. The sub-grain strengthening can be expressed as [6]

$$\Delta\sigma_{\mathrm{G}}=\frac{K_{\mathrm{y}}}{\sqrt{d_{\mathrm{g}}}} \tag{5}$$

where K_{Y} is a constant (0.14 $\mathrm{MP\cdot m^{1/2}}$ [6]), and d_{g} is the average size of sub-grains, which is 2.7 μm for the selected-DAT samples and 0.4 μm for the selected-STMT samples (measured using ImageJ software statistics of several TEM images). The sub-grain strengthening contribution of the selected-DAT samples and the selected-STMT samples is 85 and 221 MPa, respectively.

Nanoscale precipitates are dispersed during the aging treatment. The interaction between precipitates and dislocations hinders the movement of dislocations (Fig. 8(b)), increasing the strength of the alloy. The hard particles ($(\mathrm{Ni,Co})_2\mathrm{Si}$) are difficult to deform, and the interaction between precipitates and dislocations is a bypassing mechanism, i.e., the Orowan mechanism. The contribution of precipitates to strength can be expressed as [8]

$$\Delta\sigma_{\mathrm{p}}=0.81\frac{MGb}{\pi(1-\upsilon)^{1/2}}\frac{\ln(d_{\mathrm{p}}/b)}{(d_{\mathrm{p}}\sqrt{3\pi/f_{\mathrm{V}}}-2d_{\mathrm{p}})} \tag{6}$$

where d_{p} is the average size of the precipitates, which is 10 nm for the selected-DAT samples and 26 nm for the selected-STMT samples (measured using Image J software statistics of multiple TEM images); υ is Poisson ratio (0.34 [8]); f_{V} is the volume fraction of precipitates, which is 2.9% for the selected-DAT samples and 3.4% for the selected-STMT samples. The precipitation strengthening contribution of the selected-DAT samples and the selected-STMT samples is 357 and 199 MPa, respectively.

The contribution of precipitation strengthening is significantly higher for the selected-DAT samples than that for the selected-STMT samples, as reflected by the variation in microhardness. The micro-hardness of the selected-DAT samples aged at 500 °C for 480 min has an increment of HV 143, while the increment in microhardness of the selected-STMT samples is HV 79 after twice aging. The precipitates in the selected-DAT samples are uniformly nucleated with small size and hardly coarsen. In contrast, the precipitates in the selected-STMT samples are nucleated in highly defective region and coarsen easily due to stored energy introduced by deformation to improve the phase transformation driving force. This is evidenced by the fact that the aging temperature and aging time at peak microhardness decrease successively along with multi-stage thermomechanical treatment, as shown in Fig. 1. Ultimately, the strength of the selected-DAT samples lacking sub-grain strengthening and work hardening is lower than that of the selected-STMT samples.

4.2 Effect of multi-stage TMT on electrical conductivity

The electrical conductivity of alloys is governed by solid solution atoms, grain boundaries, precipitates, and dislocations. According to the Matthiessen's law, the resistivity of alloys (ρ_{alloy}) is expressed by the following equation [10,42]:

$$\rho_{\text{alloy}}=\rho_0+\Delta\rho_{\text{d}}+\Delta\rho_{\text{g}}+\Delta\rho_{\text{p}}+\Delta\rho_{\text{s}} \tag{7}$$

where ρ_0 represents the resistivity of the Cu matrix, $\Delta\rho_{\text{d}}$ represents the resistivity caused by dislocations, $\Delta\rho_{\text{g}}$ represents the resistivity caused by grain boundaries, $\Delta\rho_{\text{p}}$ represents the resistivity caused by precipitates, and $\Delta\rho_{\text{s}}$ represents the resistivity caused by solid solution atoms. Among these, the resistance caused by solid solution atoms against electron scattering is much larger than the other factors [5]. The formation and growth of precipitates are a process that decreases the solute atom content in the matrix, primarily affecting the electrical conductivity of alloys. For the selected-DAT samples, the insufficient precipitation kinetics makes it difficult for precipitates to consume solute atoms by forming and growing precipitates, resulting in low electrical conductivity. A large number of dislocations are introduced after multi-stage thermomechanical treatment. These defects provide nucleation sites for precipitates and act as diffusion channels for atoms, accelerating precipitation [6]. Besides, the stored energy introduced by the deformation acts as a driving force, enhancing the precipitation kinetics for the phase transformation. Ultimately, the selected-STMT sample has a large volume fraction of precipitates and exhibits high electrical conductivity.

4.3 Properties comparison

Figure 11 shows the tensile strength and electrical conductivity of the designed Cu−Ni−Co−Si alloy and other reported alloys [5,23,24,26,35,40, 43−47]. The composition of the studied alloys mostly adheres to a (Ni+Co)/Si mass ratio of 4−4.5. The Ni/Co mass ratio has a significant effect on the properties of the alloys. Generally, Cu−Ni−Co−Si alloys with a high Ni/Co mass ratio exhibit high tensile strength whereas those with a low Ni/Co mass ratio have good electrical conductivity. HUANG et al [5] reported Cu−4.5Ni−1.2Co−1.0Si−0.1Mg alloy with an ultra-high tensile strength of 1111 MPa and an electrical conductivity of 30.1%(IACS). OZAWA et al [24] reported Cu−1.4Ni−0.6Co−0.5Si alloy with a tensile strength of 690 MPa and a good electrical conductivity of 50%(IACS). The alloy studied in this investigation achieves excellent comprehensive properties with a tensile strength of 884 MPa and an electrical conductivity of 42.6% (IACS) (a product of tensile strength and electrical conductivity of 37.6 GP·%(IACS)) through cluster formula approach design combined with multi-stage thermomechanical treatment.

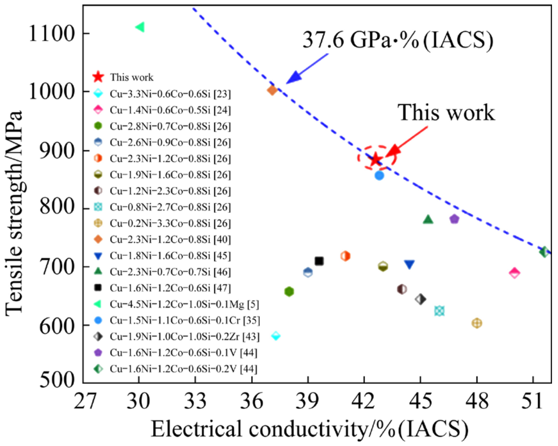

Fig. 11 Comparison of properties of Cu−Ni−Co−Si alloys with different compositions

5 Conclusions

(1) A Cu−1.9Ni−1.9Co−0.9Si alloy was designed by cluster formula approach. The alloy subjected to multi-stage thermomechanical treatment had a hardness of HV 260, a yield strength of 843 MPa, a tensile strength of 884 MPa, and an electrical conductivity of 42.6%(IACS).

(2) After multi-stage thermomechanical treatment, the grains of the alloy were refined from 2.7 to 0.4 μm, the volume fraction of $(Ni,Co)_2Si$ precipitates increased from 2.9% to 3.4%, and the dislocation density of the alloy was up to $1.6\times10^{15}\ \text{m}^{-2}$.

(3) The high strength was attributed to work hardening, sub-grain strengthening, and precipitation strengthening, with corresponding contribution of 42%, 26%, and 23%, respectively. The high electrical conductivity mainly resulted from the precipitation of a large number of nanoparticles.

CRediT authorship contribution statement

Shi-fang LI: Conceptualization, Formal analysis, Writing – Original draft; **Zhu XIAO:** Conceptualization, Validation, Writing − Review & editing; **Xiang-peng MENG:** Formal analysis; **Zhou LI:** Conceptualization, Writing − Review & editing; **Yan-lin JIA:** Conceptualization, Review & editing; **Yan-bin JIANG**: Validation, Formal analysis, Investigation.

Declaration of competing interest

The authors declare that they have no known competing financial interests or personal relationships that could have appeared to influence the work reported in this paper.

Acknowledgments

The authors acknowledge the financial support by the National Natural Science Foundation of China (No. U2202255), the Hunan Provincial Natural Science Foundation of China (No. 2024JJ2076), and the Key Research and Development Program of Ningbo, China (No. 2023Z092).

References

[1] MA Mu-zhi, XIAO Zhu, LI Zhou, JIA Yan-lin, FANG Mei, MENG Xiang-peng. Hot deformation and microstructure evolution of a Cu−Ni−Co−Si−Cr−Mg alloy [J]. JOM, 2023, 75(8): 3083−3096.

[2] ZHANG Yi, LIU Ping, TIAN Bao-hong, LIU Yong, LI Rui-qin, XU Qian-qian. Hot deformation behavior and processing map of Cu−Ni−Si−P alloy [J]. Transactions of Nonferrous Metals Society of China, 2013, 23(8): 2341−2347.

[3] QIN Liu-xin, ZHOU Tao, WANG Xu, JIANG Yan-bin, LIU Feng, XIAO Zhu, LEI Qian, JIA Yan-lin, LUO Yi, LI Zhou. Precipitation behavior of a new Cu−Ni−Co−Si−Fe−Mg alloy designed with low cobalt content [J]. Materials & Design, 2024, 240: 112833.

[4] KHEREDDINE A, LARBI F H, DJEBALA L, AZZEDDINE H, ALILI B, BRADAI D. X-ray diffraction analysis of cold-worked Cu−Ni−Si and Cu−Ni−Si−Cr alloys by Rietveld method [J]. Transactions of Nonferrous Metals Society of China, 2011, 21(3): 482−487.

[5] HUANG Jia-zhen, XIAO Zhu, DAI Jie, LI Zhou, JIANG Hong-yun, WANG Wei, ZHANG Xiao-xuan. Microstructure and properties of a novel Cu−Ni−Co−Si−Mg alloy with super-high strength and conductivity [J]. Materials Science and Engineering: A, 2019, 744: 754−763.

[6] QIN Liu-xin, ZHOU Tao, JIANG Xiao-yu, WANG Meng, HU Jin-hui, WU Zi-xiao, MENG Xiang-peng, JIANG Yan-bin, LI Zhou. Microstructure and properties of Cu−Ni−Co−Si−Cr−Mg alloy by multistage thermomechanical treatment [J]. Transactions of Nonferrous Metals Society of China, 2023, 33(12): 3739−3755.

[7] CHOI E, HAN S Z, AHN J H, SEMBOSHI S, LEE J, LIM S H. Co effect in the precipitation behavior in Cu−Ni−Si alloy [J]. Journal of Japan Institute of Copper, 2022, 61(1): 279−283. (in Japanese)

[8] ZHANG Hong-tao, FU Hua-dong, SHEN Yu-heng, XIE Jian-xin. Rapid design of secondary deformation-aging parameters for ultra-low Co content Cu−Ni−Co−Si−X alloy via Bayesian optimization machine learning [J]. International Journal of Minerals, Metallurgy and Materials, 2022, 29(6): 1197−1205.

[9] YANG Kuo, WANG Yi-han, GUO Ming-xing, WANG Hu, MO Yong-da, DONG Xue-guang, LOU Hua-fen. Recent development of advanced precipitation-strengthened Cu alloys with high strength and conductivity: A review [J]. Progress in Materials Science, 2023, 138: 101141.

[10] LI Jiang, HUANG Guo-jie, MI Xu-jun, PENG Li-jun, XIE Hao-feng, KANG Yong-lin. Effect of Ni/Si mass ratio and thermomechanical treatment on the microstructure and properties of Cu−Ni−Si alloys [J]. Materials, 2019, 12(13): 2076.

[11] LI Ying-huan, CHEN Shuai-feng, SONG Hong-wu, ZHANG Shi-hong. Enhanced mechanical properties and strengthening mechanism of Cu−Ni−Si alloy with trace chromium addition [J]. Materials Today Communications, 2024, 38: 107729.

[12] WU Ya-ke, LI Ya, LU Jun-yong, TAN Sai, JIANG Feng, SUN Jun. Effects of pre-deformation on precipitation behaviors and properties in Cu−Ni−Si−Cr alloy [J]. Materials Science and Engineering: A, 2019, 742: 501−507.

[13] LIU Qing, WANG Tong-he, JIAO Jun, WANG Wei, LIU Huan-yu, ZHANG Xiao, ZHANG Chao-xian, QI Fu-gong, JIE Jin-chuan, XU Xue-xia, DING Hai-min. The microstructures and properties of diamond reinforced Cu−Ni−Si−Ti alloys [J]. Materials Science and Engineering: A, 2023, 862: 144478.

[14] YANG Yi-hai, LI Sheng-yao, CUI Zhen-shan, LI Zhou, LI Yun-ping, LEI Qian. Microstructure and properties of high-strength Cu−Ni−Si−(Ti) alloys [J]. Rare Metals, 2021, 40(11): 3251−3260.

[15] WANG Wen-wei-jiao, WANG Jian, LI Shang-jin, WANG Chen, ZHOU Jian-hui, ZENG Jia-wei, TAN Wen-long, WANG Bing-shu. Effects of Nb addition on the properties and microstructure of Cu−Ni−Si−Mg alloy [J]. Materials Characterization, 2022, 194: 112451.

[16] LEI Qian, LI Sheng-yao, ZHU Jia-lun, XIAO Zhu, ZHANG Fei-fei, LI Zhou. Microstructural evolution, phase transition, and physics properties of a high strength Cu−Ni−Si−Al alloy [J]. Materials Characterization, 2019, 147: 315−323.

[17] WANG Wei, GUO En-yu, CHEN Zong-ning, KANG Hui-jun, CHEN Zhong-jun, ZOU Cun-lei, LI Reng-geng, YIN Guo-mao, WANG Tong-min. Correlation between microstructures and mechanical properties of cryorolled CuNiSi alloys with Cr and Zr alloying [J]. Materials Characterization, 2018, 144: 532−546.

[18] WANG Wei, KANG Hui-jun, CHEN Zong-ning, CHEN Zhong-jun, ZOU Cun-lei, LI Ren-geng, YIN Guo-mao, WANG Tong-min. Effects of Cr and Zr additions on microstructure and properties of Cu−Ni−Si alloys [J]. Materials Science and Engineering: A, 2016, 673: 378−390.

[19] ZHANG Yi, VOLINSKY A A, XU Qian-qian, CHAI Zhe, TIAN Bao-hong, LIU Ping, TRAN H T. Deformation behavior and microstructure evolution of the Cu−2Ni−0.5Si−0.15Ag alloy during hot compression [J]. Metallurgical and Materials Transactions A, 2015, 46(12): 5871−5876.

[20] WANG Zheng, LI Jiang, FAN Zhuang-zhuang, ZHANG Yi, HUI Song-xiao, PENG Li-jun, HUANG Guo-jie,

XIE Hao-feng, MI Xu-jun. Effects of Co addition on the microstructure and properties of elastic Cu−Ni−Si-based alloys for electrical connectors [J]. Materials, 2021, 14(8): 1996.

[21] LIU Feng, LI Jiang, PENG Li-jun, HUANG Guo-jiang, XIE Hao-feng, MA Ji-miao, MI Xu-jun. Simultaneously enhanced hardness and electrical conductivity in a Cu−Ni−Si alloy by addition of Cobalt [J]. Journal of Alloys and Compounds, 2021, 862: 158667.

[22] ZHAO Zhuan, ZHANG Yi, TIAN Bao-hong, JIA Yan-lin, LIU Yog, SONG Ke-xing, VOLINSKY A A. Co effects on Cu−Ni−Si alloys microstructure and physical properties [J]. Journal of Alloys and Compounds, 2019, 797: 1327−1337.

[23] LI Jiang, HUANG Guo-jie, MI Xu-jun, PENG Li-jun, XIE Hao-feng, KANG Yong-lin. Effect of Co addition on microstructure and properties of Cu−Ni−Si alloy [C]// Advances in Materials Processing. Berlin: Springer, 2018: 353−360.

[24] OZAWA A, WATANABE C, MONZEN R. Influence of Co on strength of Cu−Ni−Co−Si alloy [J]. Materials Science Forum, 2014, 783/784/785/786: 2468−2473.

[25] PENG Li-jun, MA Ji-miao, LIU Xing-yu, LIU Feng, HUANG Guo-jie, HONG Song-bai, XIE Hao-feng, YANG Zhen. Effect of heat treatment on microstructure and properties of Cu−Ni−Co−Si alloy [J]. IOP Conference Series: Materials Science and Engineering, 2019, 544(1): 012030.

[26] LI Jiang, HUANG Guo-jie, MI Xu-jun, PENG Li-jun, XIE Hao-feng, KANG Yong-lin. Influence of the Ni/Co mass ratio on the microstructure and properties of quaternary Cu−Ni−Co−Si alloys [J]. Materials, 2019, 12(18): 2855.

[27] ZHANG Jie, WANG Qing, WANG Ying-min, WEN Li-shi, DONG Chuang. Highly corrosion-resistant $Cu_{70}(Ni,Fe,Mn,Cr)_{30}$ cupronickel designed using a cluster model for stable solid solutions [J]. Journal of Alloys and Compounds, 2010, 505(1): 179−182.

[28] YU Q X, LI X N, WEI K R, LI Z M, ZHENG Y H, LI N J, CHENG X T, WANG C Y, WANG Q, DONG C. Cu−Ni−Sn−Si alloys designed by cluster-plus-glue-atom model [J]. Materials & Design, 2019, 167: 107641.

[29] LI Dong-mei, WANG Qing, JIANG Bei-bei, LI Xiao-na, ZHOU Wen-long, DONG Chuang, WANG Hua, CHEN Qing-xiang. Minor-alloyed Cu−Ni−Si alloys with high hardness and electric conductivity designed by a cluster formula approach [J]. Progress in Natural Science: Materials International, 2017, 27(4): 467−473.

[30] DONG Dan-dan, WANG Qing, DONG Chuang, NIEH T G. Molecule-like chemical units in metallic alloys [J]. Science China Materials, 2021, 64(10): 2563−2571.

[31] YANG M, HU Y L, LI X N, LI Z M, ZHENG Y H, LI N J, DONG C. Compositional interpretation of high elasticity Cu−Ni−Sn alloys using cluster-plus-glue-atom model [J]. Journal of Materials Research and Technology, 2022, 17: 1246−1258.

[32] TAKEUCHI A, INOUE A. Classification of bulk metallic glasses by atomic size difference, heat of mixing and period of constituent elements and its application to characterization of the main alloying element [J]. Materials Transactions, 2005, 46(12): 2817−2829.

[33] LIU Ke-ming, SHENG Xiao-chun, LI Xiao-long, LI Mu-lin, SHEN Zhi, FU Kai, ZHOU Hai-tao, ATRENS A. Deep cryogenic treatment characteristics of a deformation-processed Cu−Ni−Co−Si alloy [J]. Materials, 2022, 15(9): 3051.

[34] WANG Jian-wei, XIAO Xiang-peng, HUANG Guo-jie. Thermodynamic calculation of the precipitate in Cu−Ni−Si−Co alloys and experimental investigation [J]. Applied Mechanics and Materials, 2013, 423/424/425/426: 235−240.

[35] BAN Yi-jie, GENG Yong-feng, HOU Jin-rui, ZHANG Yi, ZHOU Meng, JIA Yan-lin, TIAN Bao-hong, LIU Yong, LI Xu, VOLINSKY A A. Properties and precipitates of the high strength and electrical conductivity Cu−Ni−Co−Si−Cr alloy [J]. Journal of Materials Science & Technology, 2021, 93: 1−6.

[36] LI Rong, XIAO Zhu, LI Zhou, MENG Xiang-peng, WANG Xu. Work hardening behavior and microstructure evolution of a Cu−Ti−Cr−Mg alloy during room temperature and cryogenic rolling [J]. Materials, 2023, 16(1): 424.

[37] WEI He, CHEN Yin-li, ZHAO Yi-na, YU Wei, SU Lan, TANG Di. Correlation mechanism of grain orientation/ microstructure and mechanical properties of Cu−Ni−Si−Co alloy [J]. Materials Science and Engineering: A, 2021, 814: 141239.

[38] LI Jian-qiang, ZHANG Hong-tao, SUN Jing-tai, FU Hua-dong, XIE Jian-xin. Design of low-alloying and high-performance solid solution-strengthened copper alloys with element substitution for sustainable development [J]. International Journal of Minerals, Metallurgy and Materials, 2024, 31(5): 826−832.

[39] ZHAO Zhi-lei, XIAO Zhu, LI Zhou, QIU Weng-ting, JIANG Hong-yun, LEI Qian, LIU Ze-ru, JIANG Yan-bin, ZHANG Sang-jiang. Microstructure and properties of a Cu−Ni−Si−Co−Cr alloy with high strength and high conductivity [J]. Materials Science and Engineering: A, 2019, 759: 396−403.

[40] LI Jiang, HUANG Guo-jie, MI Xu-jun, PENG Li-jun, XIE Hao-feng, KANG Yong-lin. Microstructure evolution and properties of a quaternary Cu−Ni−Co−Si alloy with high strength and conductivity [J]. Materials Science and Engineering: A, 2019, 766: 138390.

[41] WANG Lin, BHATTA L, XIONG Han-qing, LI Chang, CUI Xiao-hui, KONG Char-lin, YU Hai-liang. Mechanical properties and microstructure evolution of an Al−Cu−Li alloy subjected to rolling and aging [J]. Journal of Central South University, 2021, 28(12): 3800−3817.

[42] WANG Xu, LI Zhou, MENG Xiang-peng, XIAO Zhu. Ultrahigh strength and improved electrical conductivity in an aging strengthened copper alloy processed by combination of equal channel angular pressing and thermomechanical treatment [J]. Journal of Central South University, 2024, 31(6): 1823−1837.

[43] CHENNA KRISHNA S, SRINATH J, JHA A K, PANT B, SHARMA S C, GEORGE K M. Microstructure and properties of a high-strength Cu−Ni−Si−Co−Zr alloy [J]. Journal of Materials Engineering and Performance, 2013, 22(7): 2115−2120.

[44] ZOU Jin-feng, CHENG Jiang-yi, FENG Guang-bo, XIE Jian, YU Fang-xin. Effect of V addition on microstructure and properties of Cu−1.6Ni−1.2Co−0.65Si alloys [J]. Metals, 2019, 9(6): 679.

[45] LI Jiang, HUANG Guo-jie, MI Xu-jun, PENG Li-jun, XIE Hao-feng, KANG Yong-lin. Relationship between the microstructure and properties of a peak aged Cu−Ni−Co−Si alloy [J]. Materials Science and Technology, 2019, 35(5): 606−614.

[46] PAN Shao-bin, WANG Yong-jie, YU Jin-xin, YANG Mu-jin, ZHANG Yang-qing, WEI Hai-ting, CHEN Yue-chao, WU Jun-wei, HAN Jia-jia, WANG Cui-ping, LIU Xing-jun. Accelerated discovery of high-performance Cu−Ni−Co−Si alloys through machine learning [J]. Materials & Design, 2021, 209: 109929.

[47] DENG Li-peng, CHEN Tao, YANG Jie, LIU Feng, ZHANG Qing-ke, ZHENG Zhe-shuai, XU Cheng, SONG Zhen-lun. Evolutions in precipitates, microstructure and properties of cold-worked CuNiCoSi alloy during short-time solid solution [J]. Materials Today Communications, 2022, 30: 103150.

团簇式方法设计 Cu−Ni−Co−Si 合金的显微组织和性能

李世芳 1，肖 柱 1,2，孟祥鹏 1,3，李 周 1，贾延琳 1，姜雁斌 1

1. 中南大学 材料科学与工程学院，长沙 410083；
2. 中南大学 有色金属材料科学与工程教育部重点实验室，长沙 410083；
3. 宁波博威合金材料股份有限公司，宁波 315135

摘　要：采用团簇式方法设计了一种高强度和高电导率 Cu−1.9Ni−1.9Co−0.9Si(质量分数，%)合金。系统地研究了合金在形变热处理过程中的显微组织演变。详细讨论了合金的强化机制和电导率。最佳形变热处理工艺如下：固溶 → 80%冷轧 → (450 ℃，4 h) 时效 → 50%冷轧 → (400 ℃，4 h) 时效。合金综合性能优异，其显微硬度、屈服强度、抗拉强度和电导率分别为 HV 260、843 MPa、884 MPa 和 42.6%(IACS)。与直接时效处理相比，经多级形变热处理后，合金的晶粒得到细化、位错密度提高以及$(Ni,Co)_2Si$ 相加速析出。高强度主要归因于位错强化、加工硬化及细晶强化的共同作用，而优良的电导率则通过大量纳米颗粒的析出得以保持。

关键词：Cu−Ni−Co−Si 合金；团簇式方法；形变热处理；显微组织；强化机制

(Edited by Wei-ping CHEN)